



Cost Optimization of Electric Vertical Takeoff and Landing Aircraft Through Powertrain Modeling

Zeyu Cheng,^{*} Zhi Cao,[†] and Chris Mi[‡]
San Diego State University, San Diego, California 92182

and
John T. Hwang[§]
University of California San Diego, La Jolla, California 92023

<https://doi.org/10.2514/1.D0487>

Electric vertical takeoff and landing (eVTOL) aircraft have gained widespread attention in urban air mobility services recently. In the design of eVTOL aircraft, the powertrain system significantly impacts its performance and cost. This paper systematically describes a conceptual design and optimization methodology for eVTOL aircraft from the powertrain perspective, emphasizing its influence on overall aircraft performance and cost. The powertrain modeling methodology is achieved by considering a set of converter topologies and cutting-edge component technology, including wide-bandgap semiconductor devices, high-power-density passive components, and thermal management. Apart from that, a hybrid optimization algorithm is used in this paper to facilitate a rapid global search. Los Angeles has been selected as the example city for this study. A case study with a 30 km cruise mission range is conducted, analyzing the variation of each design variable within the optimization process. Moreover, a comparative study is implemented to illustrate the effects of the powertrain system on the eVTOL aircraft. Finally, a sensitivity analysis of the cruise mission range is presented. This paper addresses the gap in current eVTOL design methodologies from the powertrain perspective, further reducing the mission cost of eVTOL aircraft within the revenue mission profile.

Nomenclature

B_{\max}	=	maximum flux density, T	P_{core}	=	inductor core losses, W
C_{af}	=	depreciation cost of the airframe, \$	P_i	=	output power of each mission segments, W
C_{batt}	=	depreciation cost of the battery, \$	P_l	=	total losses of converter, W
C_{cap}	=	capital expense, \$	P_{px}	=	proximity losses in the winding, W
C_{elec}	=	electricity fee, \$	P_{se}	=	skin effect losses in the winding, W
C_{main}	=	maintenance cost, \$	P_{sw}	=	switching losses, W
C_{mf}	=	maintenance man-hours per flight hour	P_{winding}	=	inductor winding losses, W
C_{oss}	=	output capacitance of MOSFET, F	$R_{\text{ds,on}}$	=	turn-on resistance, Ω
C_p	=	rotor power coefficient	$R_{\text{th,hs}}$	=	heatsink thermal resistance, Ω
C_{pilot}	=	pilot cost, \$	T	=	thrust generated by one rotor, N
C_T	=	rotor thrust coefficient	t_f	=	flight hours per year, h
E_b	=	total battery energy, kWh	t_i	=	duration time of each mission segments, s
E_{rq}	=	required battery energy per mission, kWh	t_m	=	flight time per mission, min
f_{sw}	=	switching frequency, kHz	t_{off}	=	falling time of MOSFET, ns
I_{max}	=	maximum current, A	t_{on}	=	rising time of MOSFET, ns
I_{rms}	=	RMS current, A	V_{dc}	=	DC bus voltage, V
k_i	=	Steinmetz parameters	V_{ds}	=	drain-source voltage of MOSFET, V
K_s	=	slotting factor	V_t	=	the rotor tip speed, m/s
L	=	inductance, H	W	=	gross weight of aircraft, N
m_{bat}	=	battery mass, kg	W_m	=	salary per hour for mechanics, \$
m_{ind}	=	inductor mass, kg	W_p	=	salary per hour for pilots, \$
m_m	=	motor mass, kg	α	=	Steinmetz parameters
N	=	number of motors	β	=	Steinmetz parameters
N_c	=	number of battery charging cycles per day	ΔB	=	peak-to-peak magnetic flux density, T
N_m	=	number of mission tasks per day			
P_{cond}	=	conduction losses, W			

Received 6 November 2024; accepted for publication 7 March 2025; published online 27 March 2025. Copyright © 2025 by the American Institute of Aeronautics and Astronautics, Inc. All rights reserved. All requests for copying and permission to reprint should be submitted to CCC at www.copyright.com; employ the eISSN 2380-9450 to initiate your request. See also AIAA Rights and Permissions <https://aiaa.org/publications/publish-with-aiaa/rights-and-permissions/>.

^{*}Ph.D. Student, Department of Electrical and Computer Engineering.

[†]Postdoctoral Scholar, Department of Electrical and Computer Engineering.

[‡]Distinguished Professor, Department of Electrical and Computer Engineering; cmi@sdsu.edu (Corresponding Author).

[§]Associate Professor, Department of Mechanical and Aerospace Engineering. Senior Member AIAA.

I. Introduction

WITH the advancement of urbanization and increase in population density, traffic congestion and carbon emissions have become problematic. This has led to increased investment in urban air mobility (UAM), which utilizes airspace for transportation to bypass congested streets. UAM can be categorized based on application into various cases, including intracity (up to 50 km), megacity (up to 100 km), and intercity (above 100 km) [1,2]. In UAM services, electric vertical takeoff and landing (eVTOL) aircraft offer several advantages over conventional aircraft, such as environmental benefits, noise reduction, lower maintenance costs, and time savings during commutes [3]. These significant benefits have spurred extensive research into eVTOL aircraft.

Table 1 lists the previous work and their limitations. Numerous studies have examined the preliminary design and optimization of

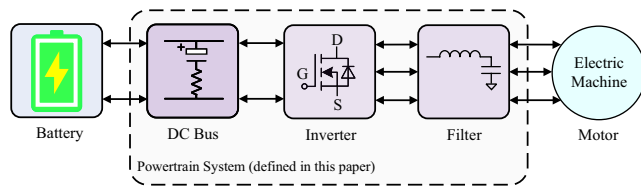
Table 1 Existing research review

Reference	Objective	Limitations
[4]	Minimize eVTOL cost per trip	Constant powertrain efficiency
[5]	Minimize eVTOL operating cost	Constant powertrain efficiency and mass
[6]	Maximize range	No powertrain model
[7]	Minimize required battery energy	No powertrain model
[8]	Minimize eVTOL gross mass	No powertrain model
[9,10]	Maximize inverter efficiency and power density	Ignore the effect of powertrain on eVTOL aircraft
Proposed model	Minimize eVTOL cost per mission	— —

eVTOL aircraft with diverse objectives [4–8]. These papers emphasize the multidisciplinary system-level design and optimization of eVTOL aircraft, taking into account factors such as aerodynamics, battery, motor, acoustics, and structural integrity. However, these studies often assess the performance of eVTOL aircraft by employing simplified powertrain models or without incorporating a powertrain system model in their optimization processes. This approach significantly diminishes the practical value of their results for both industry and researchers. Some studies, such as [9,10], optimize the powertrain system based on multiple performance criteria, including efficiency, power density, and costs. However, these studies focus solely on optimizing the powertrain itself, neglecting the impact of the powertrain system on the overall eVTOL aircraft. In powertrain optimization, it is insufficient to concentrate on the efficiency and power density of the powertrain. Since the powertrain mass constitutes only a small percentage of the total aircraft mass, it is more beneficial to consider its influence on other components of the eVTOL aircraft, such as the reliability, cost, and energy distribution on each mission segment.

This research examines the design of eVTOL aircraft from a designer perspective. The goals are to determine whether eVTOL aircraft is technically feasible, to analyze the performance of eVTOL aircraft, and to evaluate whether design remains economically viable. This paper aims to minimize the cost per mission of eVTOL aircraft by developing an in-depth powertrain model, mission model, and cost model. By optimizing costs, manufacturers can ensure that the aircraft is affordable to produce and operate, making it more attractive to potential buyers and investors. Furthermore, this paper conducts a comparison between the optimization results and a reference model that lacks a powertrain component. The purpose is to evaluate the influence of powertrain modeling on the performance of eVTOL aircraft.

This paper is organized as follows: Sec. II presents a design methodology for the powertrain model. Section III presents the

**Fig. 1** Powertrain system.

detailed description of the optimization routine, mass model, and mission profile model. The model validation, comparison, and parameter sensitivity analysis are given in Sec. IV. Finally, conclusions are presented in Sec. V.

II. Powertrain Modeling Methodology

This section describes the design and modeling methodology for converter topologies, semiconductor devices, inductors, capacitors, and cooling systems. Figure 1 illustrates the schematic of the powertrain system analyzed in this study. The powertrain system follows the architecture used in all-electric aircraft (AEA) [11]. The battery pack connects to the inverter, which then connects to the motor. It should be noted that the motor is not included in this powertrain architecture due to its complex modeling methodology.

A. Power Converter Topology Selection

Based on the configurations, sizes, and power demands of eVTOL aircraft, choosing different converter topologies and powertrain architecture is extremely important. Figure 2 depicts the main schematic of the studied topologies.

Three inverter topologies are evaluated in this paper: two-level (2L) inverter, three-level active neutral point clamping (3L-ANPC) inverter, and three-level T-type (3L-T) inverter, presented in Figs. 2a, 2b, and 2c, respectively. All inverter topologies are operated using sinusoidal pulse width modulation (SPWM).

The selection of semiconductor devices plays a significant role in the performance of the powertrain. In this paper, only wide-bandgap (WBG) devices are studied due to their high efficiency, high voltage rating, and high operating frequency. Different converter technologies, voltage ratings, and the number of parallel devices are considered and optimized in this study. Table 2 lists all the power devices considered in this paper, along with their parameters. It is important to note that all devices are assumed to operate under constant temperature conditions. The conduction losses and switching losses can be expressed as

$$P_{\text{cond}} = I_{\text{rms}}^2 R_{\text{ds,on}} \quad (1)$$

$$P_{\text{sw}} = \frac{1}{2} C_{\text{oss}} V_{\text{ds}}^2 + \frac{1}{6} V_{\text{ds}} I_{\text{rms}} f_{\text{sw}} (t_{\text{on}} + t_{\text{off}}) \quad (2)$$

where $R_{\text{ds,on}}$ is the turn-on resistance of the semiconductor devices, C_{oss} is the output capacitance, and t_{on} and t_{off} are the rising and

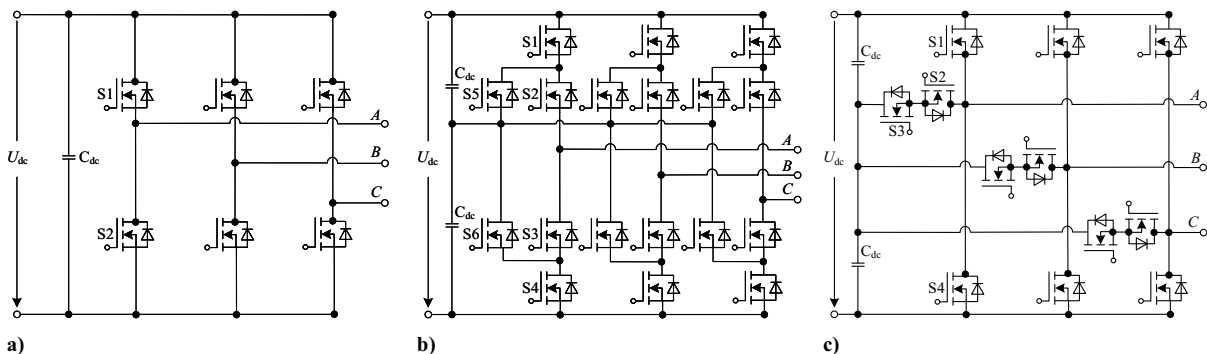
**Fig. 2** Main considered converter topologies: a) two-level inverter, b) three-level ANPC inverter, and c) three-level T-type inverter.

Table 2 Semiconductor devices used in this study

Part no.	Manufacturer	Tech.	$V_{ds,max}$	R_{on}	I_d	$R_{th,j}$	C_{oss}	t_{on}	t_{off}
G3R12MT12K	GeneSiC	SiC	1.2 kV	12 mΩ	157 A	0.26°C/W	284 pF	34 ns	22 ns
BSM180D12P2C101	Rohm	SiC	1.2 kV	11 mΩ	204 A	0.11°C/W	1500 pF	80 ns	80 ns
TP65H015G5WS	Transphorm	GaN	650 V	18 mΩ	93 A	0.47°C/W	307 pF	18 ns	9.4 ns
GA50JT06-258	GeneSiC	SiC	600 V	25 mΩ	100 A	0.26°C/W	284 pF	33 ns	44 ns
IGO60R070D1AUMA1	Infineon	GaN	600 V	70 mΩ	31 A	1°C/W	72 pF	8 ns	15 ns

falling times, respectively. These four parameters are extracted from the datasheet. V_{ds} is the drain-source voltage, f_{sw} is the switching frequency, and I_{rms} is the rms current through the device.

B. Inductor

The design of an inductor consists of two main components: magnetic component design and winding design. In the magnetic component design, various core shapes and magnetic materials are compared and optimized in this study. Theoretically, the high power density of an inductor is primarily determined by the ratio of saturation flux density to mass density. Consequently, amorphous materials exhibit the highest power density compared to other materials [12]. However, in high-frequency applications, amorphous cores have relatively higher core losses compared to other materials due to their high saturation flux density [13,14]. Therefore, different core materials are compared and selected based on the specific converter topologies and operating conditions.

The magnetic equivalent circuit (MEC) and nonlinear iteration method are utilized to calculate the magnetic flux density in different regions [15]. The improved generalized Steinmetz equation (iGSE) [16] is then applied to calculate the core losses P_{core} :

$$P_{core} = \frac{1}{T} \int_0^T k_i \left| \frac{dB}{dt} \right|^2 (\Delta B)^{\beta-\alpha} dt \quad (3)$$

where α , β , and k_i are Steinmetz parameters [17,18]; ΔB represents the peak-to-peak magnetic flux density in each region.

The design of the winding depends on factors such as current density, core shape, and saturation flux density. A constant current density is assumed to further determine the winding diameters. To avoid the saturation effect, the number of turns N can be calculated using Eq. (4). The winding constraint equation is given by Eq. (5), which states that the total copper area must be less than the slot area W_{slot} . A constant slotting factor K_s of 0.7 is assumed.

$$N = \frac{I_{max}L}{B_{max}A_c} \quad (4)$$

$$2NA_w \leq K_s W_{slot} \quad (5)$$

where I_{max} is the maximum current, L is the inductance, B_{max} is the saturation flux density, and A_c is the cross-sectional area.

Litz wire is the only type considered in this study, due to its lower winding losses compared to other types of winding. The analytical model for winding losses, which takes into account the skin effect and proximity [19], is shown in Eqs. (6) and (7).

$$P_{se} = nR_{dc}F_R(f) \left(\frac{I_L}{n} \right)^2 \quad (6)$$

$$P_{px} = nR_{dc}G_R(f)(\hat{H}_e^2) \quad (7)$$

where n is the number of strands; R_{dc} is the winding DC resistance; $F_R(f)$ is a factor that describes the increase of DC resistance due to skin effect; and \hat{H}_e is the peak of the external magnetic field.

C. Capacitor

Ceramic and film capacitors are considered in this paper due to their high power density and light weight. The method for estimating the mass of capacitors is detailed in Eq. (8):

$$m_{cap} = kV_r^\alpha C^\beta V_c \quad (8)$$

where k , α , and β are parameters related to different types of capacitors and can be found in [20]. The capacitance C , voltage rating V_r , and volume of the capacitor V_c can be extracted from the datasheet.

D. Heatsink

Both air-forced cooling [21] and single-phase liquid cooling systems [22] are considered in this study. The optimizer evaluates each cooling method during the optimization process to determine which one results in the minimum heatsink mass while satisfying the thermal constraints. The thermal resistance of the heatsink is calculated using the thermal equivalent circuit method, while the thermal resistance of each semiconductor is extracted from its datasheet. The heatsink geometry and fan characteristics are taken into account in the cooling system models. The maximum allowed heatsink thermal resistance is calculated using Eq. (9):

$$R_{th,hs} = \frac{T_{hs} - T_{amb}}{P_l} \quad (9)$$

where T_{hs} is the maximum allowed heatsink plate temperature, restricted to 105°C; T_{amb} is the maximum ambient temperature, limited to 35°C; and P_l is the total power loss of the converter. The mass of the heatsink is calculated based on its geometry.

III. Single Objective Optimization

A. Optimization Routine

The optimization tool developed in this study targets the cost per mission of eVTOL aircraft as the objective, considering all relevant degrees of freedom (DOF) in the powertrain system and mission profile. The optimization process employs a hybrid algorithm that integrates the genetic algorithm with the simulated annealing algorithm (GASA). GASA maintains the rapid global search capability of GA and the local space exploration capability of SA, thereby preventing the optimization trapped in multilocal optimum solutions. The lift + cruise aircraft configuration is analyzed in this study, as illustrated in Fig. 3. The design variables, along with other constant inputs, are summarized in Table 3. The bound range of

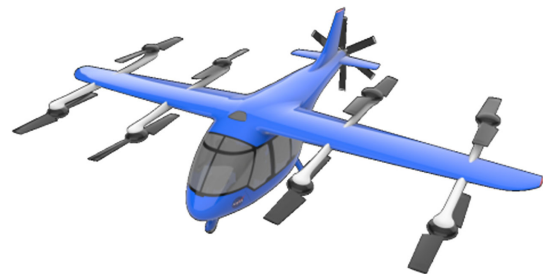


Fig. 3 NASA Lift + Cruise eVTOL aircraft configuration [23].

Table 3 Design variables and constant inputs

Model	Design variable	Variable range	Constant parameters
Powertrain model	Switching frequency, f_{sw}	[10 kHz, 200 kHz]	Motor electric frequency
	DC bus voltage, V_{dc}	[800 V, 1400 V]	Considered semiconductors
	Rated output power, P_o	[5 kW, 200 kW]	Core material property
	Winding diameter, d_i	[1.4 mm, 4.6 mm]	Capacitor Pk-Pk voltage ripple
	Inductor geometry variables		
	Heatsink geometry variables		
	Ripple attenuation factor, RAF	[0, 1]	
	Inverter converter topologies, T_i	[1, 3]	
Mass model	Battery mass, m_{bat}	[200 kg, 800 kg]	Listed in Table 4
Mission model	Maximum range, R_{max}	[30 km, 100 km]	Listed in Table 4

converter topologies is defined by the number of converters included in this optimization. The objective function can be written as (10)

$$\begin{aligned}
 &\text{Minimize } Cost_m = f(\mathbf{x}) \\
 &\text{Subject to } p_i(\mathbf{x}) \leq 0, i = 1, \dots, n_p \quad (10) \\
 &\quad \quad \quad m_i(\mathbf{x}) = 0, i = 1, \dots, n_m
 \end{aligned}$$

where $f(\mathbf{x})$ is the objective function, subject to n_p inequality constraints $p_i(\mathbf{x})$ and n_m equality constraints $m_i(\mathbf{x})$. The detailed optimization routine is illustrated in Fig. 4.

B. Mass Model

The mass model of the eVTOL aircraft is divided into four components: powertrain mass, battery mass, airframe mass, and motor mass. Motor mass is assumed to be constant in this study. The airframe mass is estimated using a constant ratio of the airframe mass to the overall mass of the aircraft. The mass of the powertrain model is the sum of all subcomponent mass, as described in Sec. II. The battery mass is considered as a design variable in this optimization problem. The input parameters are listed in Table 4.

Table 4 Input parameters of mission model and mass model

Model	Parameter	Value
Mission model	Cruise mission range	30 km
	Pilot mass	75 kg
	Passengers	3
	Mass per passenger	90 kg
	Reserve time	20 min
	Boarding time	15 min
	Hover time in sizing mission	2 min
	Hover time in revenue mission	0.5 min
	Cruise speed	124 km/h
	Lift to drag ratio	10
	Motor efficiency	95%
	Propeller efficiency	85%
	Mass model	Ratio of airframe mass to gross mass
Motor mass		25 kg
Number of motors		8
Battery energy density		400 Wh/kg

C. Mission Model

The mission model considers the sizing mission profile and the revenue mission profile. The sizing mission profile mainly emphasizes the preliminary design of eVTOL aircraft, the completion of mission tasks, and the estimation of the maximum mile range of

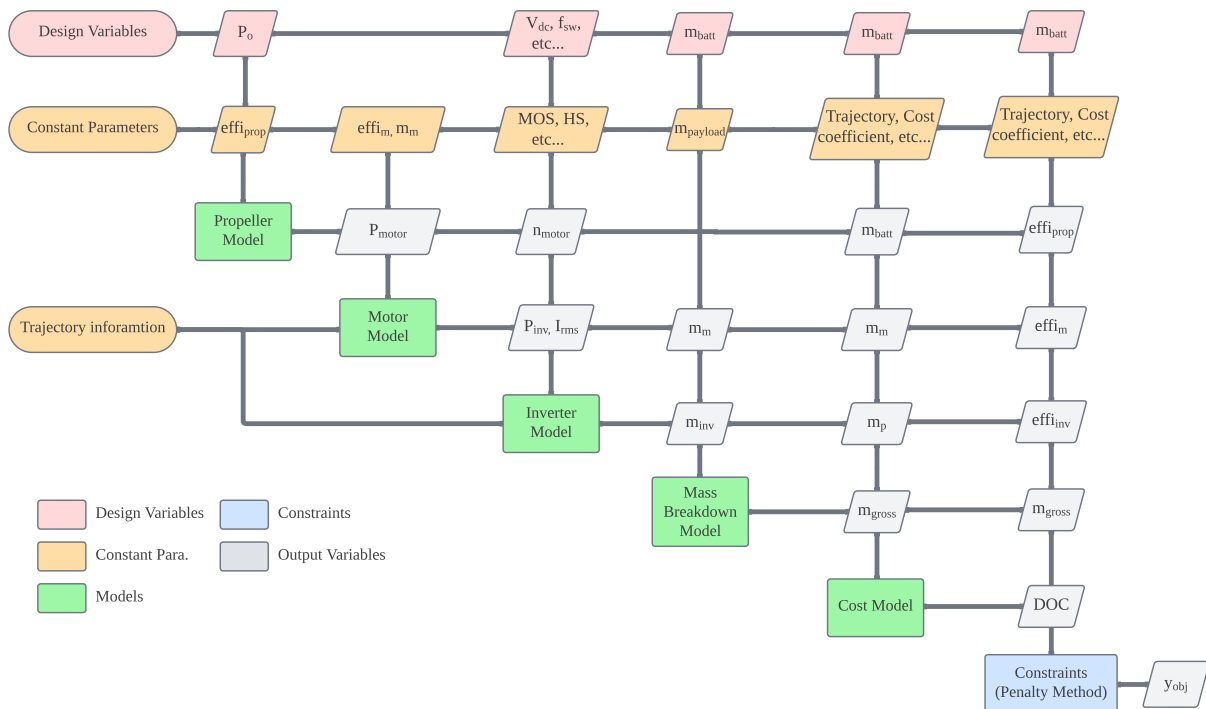


Fig. 4 Optimization flowchart.

Downloaded by Politecnico di Milano on July 26, 2025 | http://arc.aiaa.org | DOI: 10.2514/1.D00487

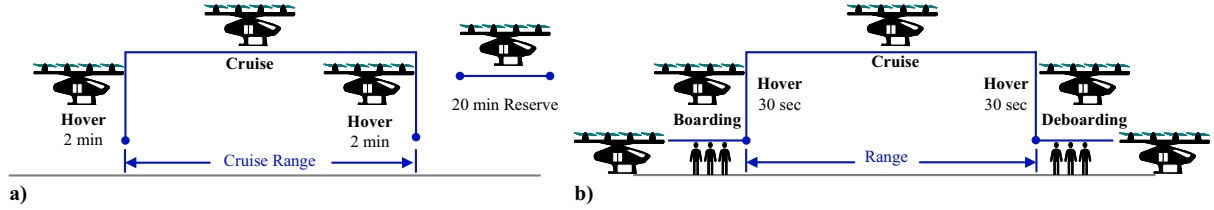


Fig. 5 a) Sizing mission profile. b) Revenue mission profile.

eVTOL aircraft. The revenue mission profile is aimed at assessing the market revenue potential of future business services and estimating the cost of eVTOL aircraft within a given business model.

A diagram of both mission profiles is shown in Fig. 5. The sizing mission profile includes the cruise, hover, and reserve mission segments. The reserve segment is typically utilized as additional battery capacity or flight time for safety reasons, handling the emergency situation during the flight. A 20 min reserve time is included in the mission model, following the requirement of visual flight rules (VFR) by the FAA [24]. Moreover, the reserve speed needs to be adjusted due to the loiter requirement from the FAA. The adjustment method could be found in [4]. It should be noted that while the current analysis focuses on the primary mission segments of hover, cruise, and reserve, the optimization framework is inherently flexible and capable of incorporating additional phases such as climb and descent. However, for clarity and simplicity, the climb and descent phases are not included in the following analysis, while noting that the approach can be extended to accommodate them as needed.

The revenue mission profile includes cruise, hover, and boarding mission segments. The boarding segment allows for activities such as passenger loading, unloading, and safety checks, among others. Concurrently, the battery is charged during this time. Constant boarding is assumed in the revenue mission model. The input parameters of the mission model are presented in Table 4.

In order to analyze the performance of the powertrain throughout the entire mission profile, the power demand for each mission throughout the entire mission profile, the power demand for each mission throughout the entire mission profile, the power demand for each mission throughout the entire mission profile, the power demand for each mission throughout the entire mission profile, as described in (11). The power of propellers in the hover segment can be calculated using Eq. (12) based on momentum theory.

$$NT - W = 0 \quad (11)$$

$$P_h^r = \frac{C_p}{C_T} V_t T \quad (12)$$

where T is the thrust generated by the single rotor, N is the number of rotors, W is the gross weight of aircraft, C_T and C_p are the thrust coefficient and rotor power coefficient, and V_t is the rotor tip speed.

In the cruise and reserve mission segments, the required output power of the inverter can be calculated using Eq. (13). Due to the loiter adjustment in the reserve segment, the L/D ratio of the reserve needs to be adjusted accordingly [4].

$$P_{inv}^i = \frac{WV_i}{(L/D)_i \eta_m \eta_p}, \quad i = \text{cruise, reserve} \quad (13)$$

where P_{inv}^i represents the required output power of the inverter, W is the gross weight of the eVTOL aircraft, L/D is the aircraft's lift-to-drag ratio, η_m denotes the motor efficiency, and η_p is the propeller efficiency.

Apart from that, the efficiency and power distribution inside the powertrain system can be further calculated using the powertrain model and the given constant motor efficiency in Table 4. Subsequently, the used battery energy in each mission segment can be calculated using Eq. (14).

$$E_i = \frac{P_i t_i}{\eta_i} \quad (14)$$

where i represents the different mission segments; P_i and η_i represent the output power and efficiency of the powertrain, respectively; while t_i is the flight time of each mission segment.

An equality constraint is used in the mission model, as shown in Eq. (15), to ensure appropriate energy distribution throughout the mission task.

$$E_b - (E_h + E_c + E_r) = 0 \quad (15)$$

where E_b represents the total battery energy, E_h is the energy used in the hover segment, E_c is the energy used in the cruise segment, and E_r is the energy used in the reserve segment.

Since the battery mass is considered as a design variable, the total battery energy E_b can be calculated by multiplying the battery mass by the constant battery energy density provided in Table 4.

D. Direct Operating Cost Model

The direct operating cost (DOC) model in this study is based on the most recent DOC methods [4,25,26]. These methods were chosen due to their minimal input requirements and comprehensive estimation of all relevant DOC elements, including capital expense, maintenance cost, and flight cost. However, since the DOC models in [25,26] are designed for conventional or hybrid aircraft, modeling adjustments are necessary for AEA. Moreover, although [4] developed a DOC model for eVTOL aircraft, the capital expense in [4] neglects the residual value of each component and the annual replacement cost of the battery. In this study, several adaptations have been made, and the newest input parameters have been updated accordingly.

The DOC model in this paper is subdivided into three categories: capital expense, maintenance cost, and flight cost. Table 5 lists all input parameters used in the DOC model. Based on data from the FAA [27], the 2018 average hourly wage in the aircraft manufacturing industry was \$42.11. Considering indirect costs ranging and additional benefits, the fully burdened wrap rate is estimated to range between \$115 and \$153 per hour. In this paper, the average value is used to represent the pilot's average wrap rate.

Capital expense includes the depreciation cost of the airframe, avionics system, and battery. The purchase price and residual value of each component are considered. The cost equations are presented in Eqs. (16–18).

Table 5 DOC model input parameters

Parameter	Value	Source
Airframe purchase price	\$1102 per kg	[4]
Airframe residual value	10%	[28]
Avionics purchase price	\$100,000	[4]
Avionics residual value	10%	[28]
Battery purchase price	\$200 per kWh	[29]
Battery residual value	40%	[30]
Battery cycle life	1000 cycles	[31]
Price of electricity	\$0.16	[32]
Maintenance/flight hour	60%	[33]
Mechanic wrap rate	\$62 per hour	[34]
Pilot wrap rate	\$134 per hour	[27]
Pilots per aircraft	1	—

$$C_{af} = \frac{\text{Airframe price} - \text{Residual}}{\text{Years} \times M_i} \quad (16)$$

$$C_{av} = \frac{\text{Avionics price} - \text{Residual}}{\text{Years} \times M_i} \quad (17)$$

$$C_{batt} = \frac{1}{M_i} \times \sum_{i=1}^{N_i} \frac{\text{Battery price} - \text{Residual}}{\text{Cycle life}} \times \text{cycle}_i \quad (18)$$

where M_i is the number of mission times per year and N_i is the number of the replaced battery per year.

The calculation of N_i is based on Eqs. (19–21). It is assumed that the yearly flight hours are evenly distributed throughout the days.

$$N_m = \frac{t_f}{365} \times \frac{1}{t_m} \quad (19)$$

$$N_c = \frac{N_m}{E_b/E_{rq}} \quad (20)$$

$$N_i = \frac{365}{\text{cycle life}/N_c} \quad (21)$$

where N_m is the number of mission tasks per day; t_m is the flight time per mission; t_f is the flight hours per year; E_b is the total battery energy of the aircraft; E_{rq} is the required battery energy per mission; and N_c is the number of battery charging cycles per day.

The airframe purchase price is based on the investigation in [4], and a 10% residual value for the airframe and avionics is assumed in this paper [28]. The eVTOL aircraft is assumed to operate for 2000 h per year over a span of 5 years before retirement, leading to a 10,000 h service time. For comparison, the business aircraft are typically operated around 500–2000 h per year [35]. According to [29,30], the price of a new EV battery is around \$150–\$200 per kWh, and the estimated price of second-life batteries is expected to be 30%–70% of the new battery price in 2025. As a compromise, an estimated \$200 per kWh and a 40% battery residual value are used in this study. The battery cycle life is defined as the number of cycles until the state of health (SOH) of the battery reaches 70%–80% of its nominal value. The current state-of-the-art life cycles can be up to 1000 [31], which is the assumption used in this paper.

The maintenance cost is calculated using Eq. (22). A 0.25–1 maintenance man-hours per flight hour is normally utilized in light aircraft [33]; \$53–67 per hour is typical for general aviation mechanics [33].

$$C_{main} = \frac{1}{M_i} \times C_{mf} \times W_m \times t_f \quad (22)$$

where C_{mf} is a fixed value of maintenance man-hours per flight hour, depending on the size of aircraft, and W_m is the salary per hour for mechanics.

The flight cost includes the pilot cost and energy cost. Pilot costs are calculated using Eq. (23); \$70–120 per hour is typical for business pilots [33]. Electricity cost is calculated using Eq. (24). The amount of electricity per year can be evaluated by the powertrain model.

$$C_{pilot} = \frac{1}{M_i} \times N_p \times W_p \times t_f \quad (23)$$

$$C_{elec} = \frac{1}{M_i} \times E_{am} \times p_e \quad (24)$$

where N_p is the number of pilots per aircraft; W_p is the salary per hour for pilots; E_{am} is the amount of electricity per year; and p_e is the price of electricity per kWh.

IV. Results and Discussion

A. Powertrain Model Validation

The powertrain model has been validated through a comparison with simulation results obtained from the PSIM software. A 60 kW 3L-ANPC inverter was used to validate the powertrain model. The nonideal thermal switch model was utilized in this simulation. Figure 6a shows the efficiency comparison between the proposed powertrain model and the PSIM simulation, and the absolute error is also presented in this figure. In the 10 kW case, due to the nonlinear effect on the switching losses, the powertrain model cannot estimate efficiency accurately. The absolute errors at higher power levels are similar. This is because the core losses of each inductor are only considered in the proposed powertrain model. The errors in switching losses and conduction losses gradually increase with higher power demand. Figure 6b illustrates the loss breakdown in the powertrain model, where the switching and conduction losses constitute the majority of the power losses. The inductor core loss is validated by Ansys Maxwell software. Figure 6c shows the comparison of core losses under different loads between the analytical model (AM) and Ansys Maxwell's simulation. MnZn ferrite N87 material was used. Its datasheet and parameters are detailed in [17].

B. Optimization Results

In order to provide a more practical value for industry through this optimization, a real case has been studied in this paper. Los Angeles City was selected as an example city for the implementation of UAM service [36]. Air taxi service has already existed in the city and is mainly operated by companies such as Blade and Orbic Air. Orbic Air provides the heliport airport transfer services between Los Angeles International Airport (LAX) and Burbank Airport. The flight distance between the two airports was around 18.5 mi (30 km). The flight time is around 10–15 min [37].

In this case, a 30 km distance and a 15 min flight time were selected for the revenue mission profile in this optimization problem. Another 15 min is allocated for the boarding segment. The total mission time for a single trip is approximately 30 min. The input data for this optimization study is provided in Tables 3 and 4. The

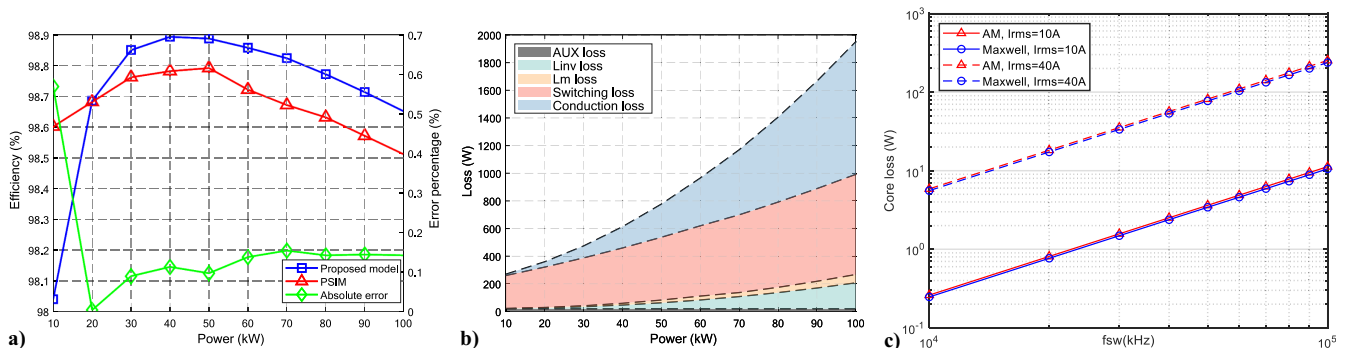


Fig. 6 Validation results. a) Efficiency. b) Loss breakdown. c) The comparison of core losses between AM and Maxwell.

key results of the cost optimization are demonstrated in Fig. 7, where the masses of the powertrain, battery, airframe, and payloads are considered.

Figure 7a shows the optimization results for cost minimization. The GA algorithm is solely utilized to rapidly explore the design space for potential optimal solutions in the first 400 generations. After that, the GA algorithm combined with the SA algorithm is used to efficiently find the potential global optimal solution due to the existence of multiple local optimum solutions. The cost per mission gradually decreases and converges at \$183.5 per mission. Since most of the design variables are close to convergence before 1200 generations, Figs. 7b–7d only illustrate the results of each component before 1200 generations.

Figure 7b shows the mass breakdown of the eVTOL aircraft in this optimization problem. Each component's mass of eVTOL aircraft is gradually reduced and converged. Figure 7c shows the DOC breakdown and power distribution along each mission segment. Since the costs of pilot, maintenance, and avionics are fixed in this optimization, only the depreciation cost of the airframe and battery and the cost of electricity are presented, which are gradually reduced due to the reduction of airframe mass and battery mass. In addition, the reserve segment has the lowest required power due to the loiter adjustments discussed in Sec. III.B. The hover segment has the highest power and lowest efficiency.

Figure 7d demonstrates the variation of design variables during the optimization process. The 3L-ANPC inverter is selected since it theoretically has the highest efficiency among all inverter topologies in high-power and high-voltage applications. The switching frequency and DC bus voltage converge at 111 kHz and 1400 V, respectively. This would be the optimal selection by the optimizer, considering the tradeoff between powertrain efficiency and the total system cost. A higher switching frequency would reduce the mass of passive components but also increase losses and battery mass, which further increase the battery cost and cost per mission of the eVTOL aircraft. The DC bus voltage approaches the upper bound mainly because conduction losses can be reduced at the same power level of the powertrain system. The maximum mission range converges at 30 km, indicating that the eVTOL aircraft achieves the minimum operating cost when the cruise range of the sizing mission profile matches the range of the revenue mission profile. The battery

mass converges at 589 kg. The other design variables have converged at certain levels, and none of the constraints are violated in the final optimization results.

C. Comparison Study

The comparison study is conducted to illustrate the impacts of the powertrain system on the operating cost of eVTOL aircraft. The baseline model is based on the optimized results in [4], which uses the cost per trip as the objective and provides detailed input parameters and analysis of results. However, the baseline model does not include a detailed powertrain model. Instead, it relies on simplified assumptions for the analysis of eVTOL cost. For example, at each stage of the powertrain (inverter, motor, and battery), the efficiency is assumed to be constant and representative of typical values found in literature or industry standards. Furthermore, the reference model does not account for detailed interactions or dynamic behavior between powertrain components. It simply assumes that energy is delivered through the system with these fixed efficiencies. These simplifications highlight a key limitation of the reference model. In this case, this study uses the same input parameters of the lift + cruise eVTOL aircraft referenced in [4] and focuses on optimizing the cost per mission of the eVTOL aircraft from a more detailed powertrain perspective. Finally, a comparison is made between the cost per mission of the eVTOL aircraft, the capital expense, crew cost, maintenance cost, and electricity cost. It should be noted that, since the motor mass and powertrain mass are neglected in [4], these masses are also ignored in this comparative study.

Figure 8a indicates that battery mass is 8.15% lighter than the reference battery mass. Figure 8b demonstrates that the depreciation cost of the airframe is 8.6% less than the reference cost. Additionally, powertrain optimization can achieve a 13% reduction in the depreciation cost of the battery, a 13% reduction in electricity fees, and a 6.6% reduction in total DOC, compared to the reference model. These improvements result from enhanced powertrain efficiency and optimized power distribution in each segment. Theoretically, this is valid because the overall efficiency of the electric system is increased through powertrain optimization, leading to a reduction in the total required battery energy. Apart from that, trajectory optimization contributes to the reduction of battery mass.

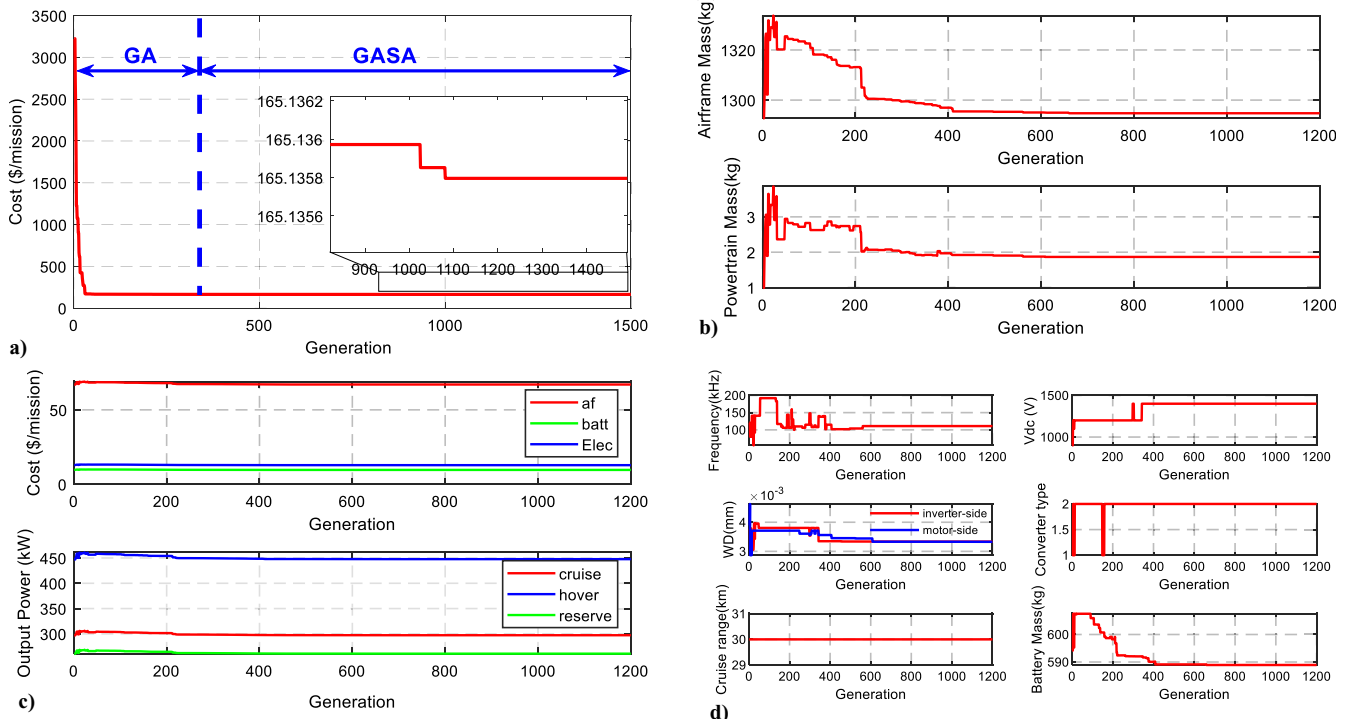


Fig. 7 Results from the configuration study. a) Cost per mission. b) Mass breakdown. c) Cost breakdown and power distribution. d) Design variables variation.

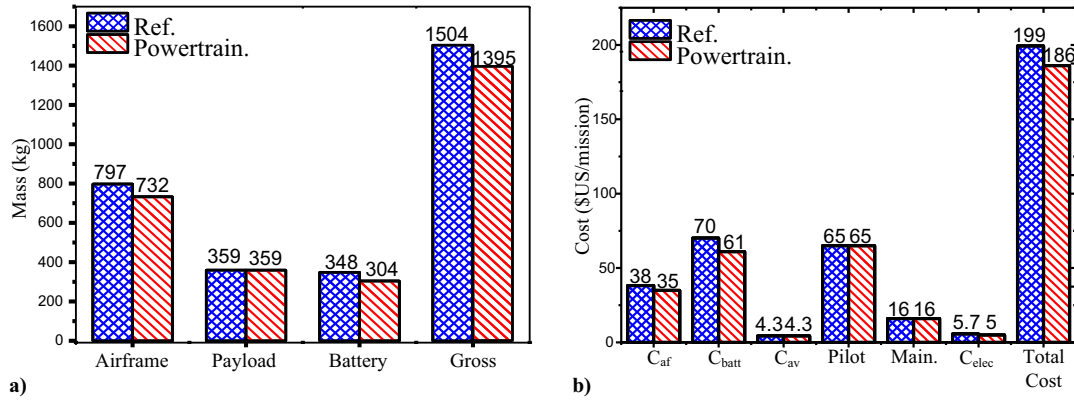


Fig. 8 Results from the comparison study. a) Mass breakdown. b) DOC breakdown.

When the battery mass is reduced due to improved efficiency, the gross weight of the aircraft decreases accordingly. Consequently, the range constraints in Eq. (13) are not satisfied with the reduced gross weight. Equation (13) can therefore be reformulated as Eq. (25).

$$\text{Range}_i = \eta_{\text{sys},i} \frac{L}{D} \frac{P_i t_i}{W} = \frac{L}{D} \frac{P_i t_i}{W} \quad (25)$$

The range constraints are directly related to the output power in each segment and the gross weight of the aircraft. When the gross weight is reduced, the optimizer must decrease the output power in each segment to maintain a constant range, leading to a further reduction in battery mass. Additionally, the reduction in airframe mass also contributes to the total mass reduction in the final optimization results due to the fixed airframe mass ratio. Consequently, capital expenses are reduced because of the decreased airframe mass and battery mass.

D. Sensitivity Analysis

The sensitivity of the revenue cruise mission range is analyzed by varying the cruise mission range and optimizing the cost per mission of the eVTOL aircraft accordingly. The same input parameters and

optimization routine described in Sec. III are utilized in this study. The main results are presented in Figs. 9 and 10.

Figures 9a and 9b demonstrate the variation of DOC and the gross mass of eVTOL aircraft with respect to the cruise mission range. A comparison study between models with and without the powertrain model is also illustrated. With the increment of the cruise mission range, the effect of the powertrain on both DOC and the gross mass of the eVTOL aircraft becomes increasingly significant. Figure 9c illustrates the cost breakdown and variations of each cost component with the increasing cruise mission range. The comparison study is also included in this diagram. The cruise range has a more significant impact on the electricity cost and depreciation cost of the battery. Moreover, Fig. 9d presents the variations of output power across different mission segments, with a comparison between models with and without a powertrain. The optimization of the required power of the powertrain in each mission segment is accomplished through the powertrain model.

Figure 10a presents the battery mass variation with respect to the cruise mission range. As the mission range increases, higher energy is required, and thus the battery mass must be increased. The comparative study shows that the powertrain gradually has a more significant impact on the performance of the aircraft as the mission range increases. Figure 10b demonstrates the variations in powertrain mass.

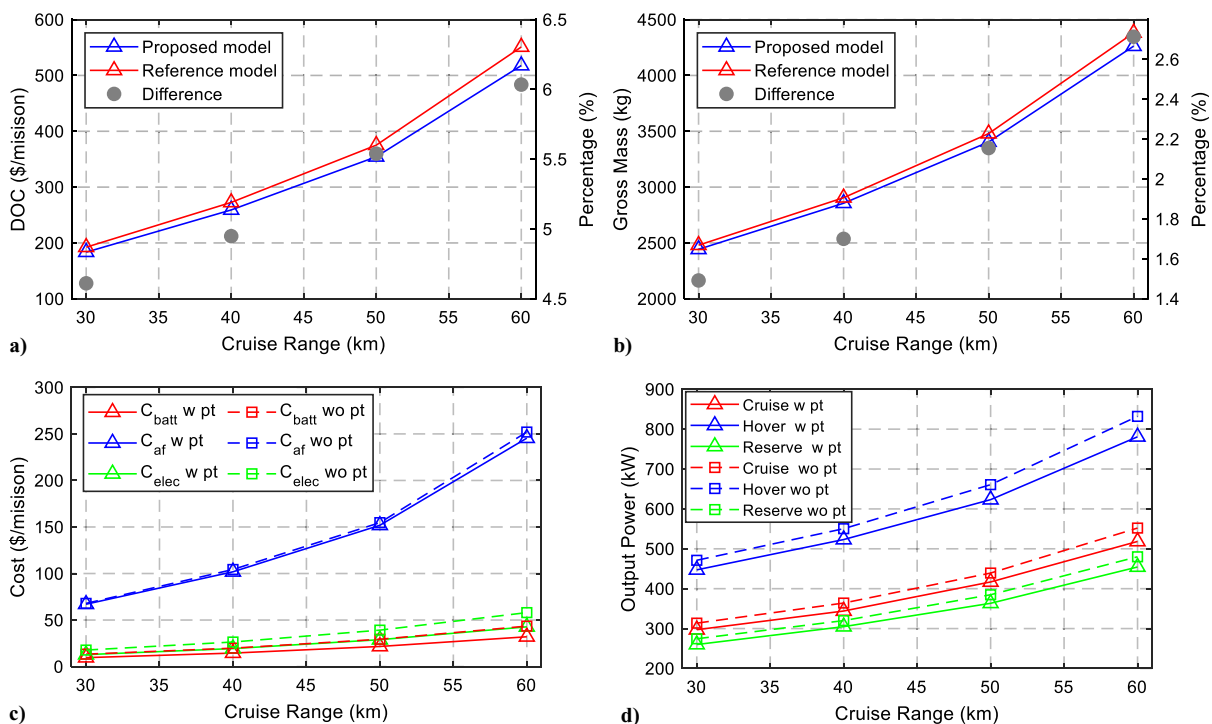


Fig. 9 Sensitivity to cruise range. a) DOC. b) Gross mass. c) Depreciation and electricity cost. d) Power demand of segment.

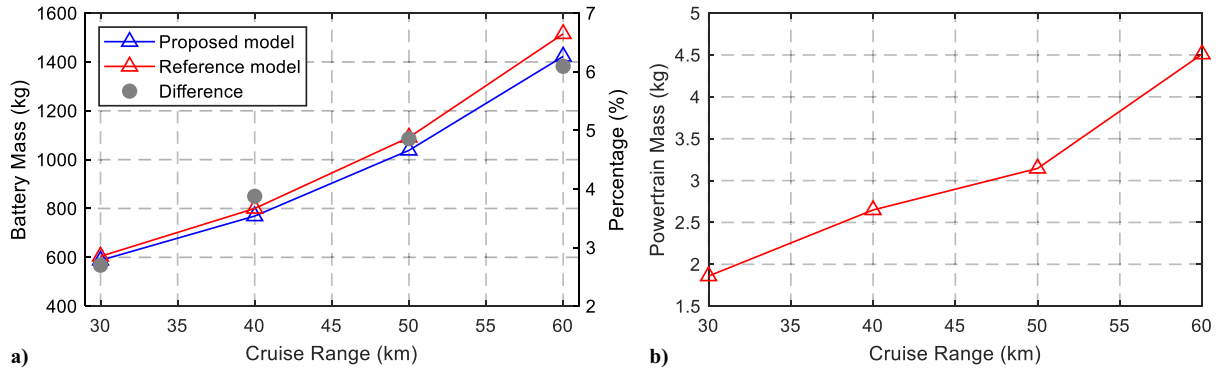


Fig. 10 Sensitivity to cruise range. a) Battery mass. b) Powertrain mass.

Figures 11a and 11b show the variation of the main design variables with the increasing cruise range. As the distance increases, the optimal design undergoes changes, primarily in terms of output power. Due to the increase in distance, the battery weight and the aircraft body weight increase, which requires the motor to produce larger power to deliver the necessary torque. For the powertrain model, as the voltage has already reached the preset maximum value, the current gradually increases, necessitating the use of thicker wires and more effective cooling methods to satisfy the constraints of heat dissipation and current density. That is why the winding diameter increases with the increasing cruise range. Furthermore, the conduction losses are increased. To maintain high

efficiency of the powertrain, the optimizer captures this characteristic and gradually decreases the switching frequency to compensate for the increase in conduction losses.

Figure 12 shows that the variation of DOC, gross mass of eVTOL aircraft, cost of each subcomponent, output power of each mission segment, and battery and powertrain mass decrease as battery energy density increases. However, it should be noticed that as battery and energy density increase, the rate of reductions in DOC and gross mass decreases. This indicates that the contribution of the battery to the DOC and gross mass of aircraft is reducing, while components such as the aircraft airframe, maintenance staff, and pilot salaries become the dominant contributors to the DOC. This

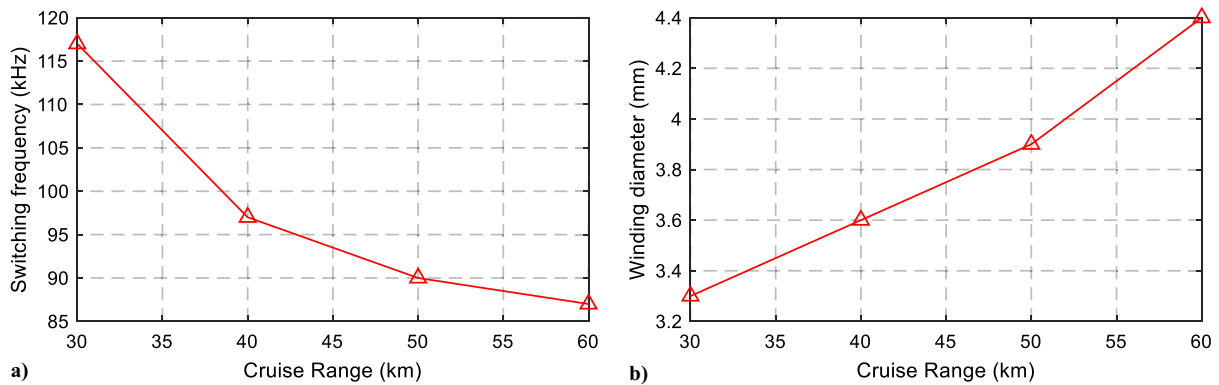


Fig. 11 Sensitivity to cruise range. a) Switching frequency. b) Winding diameter.

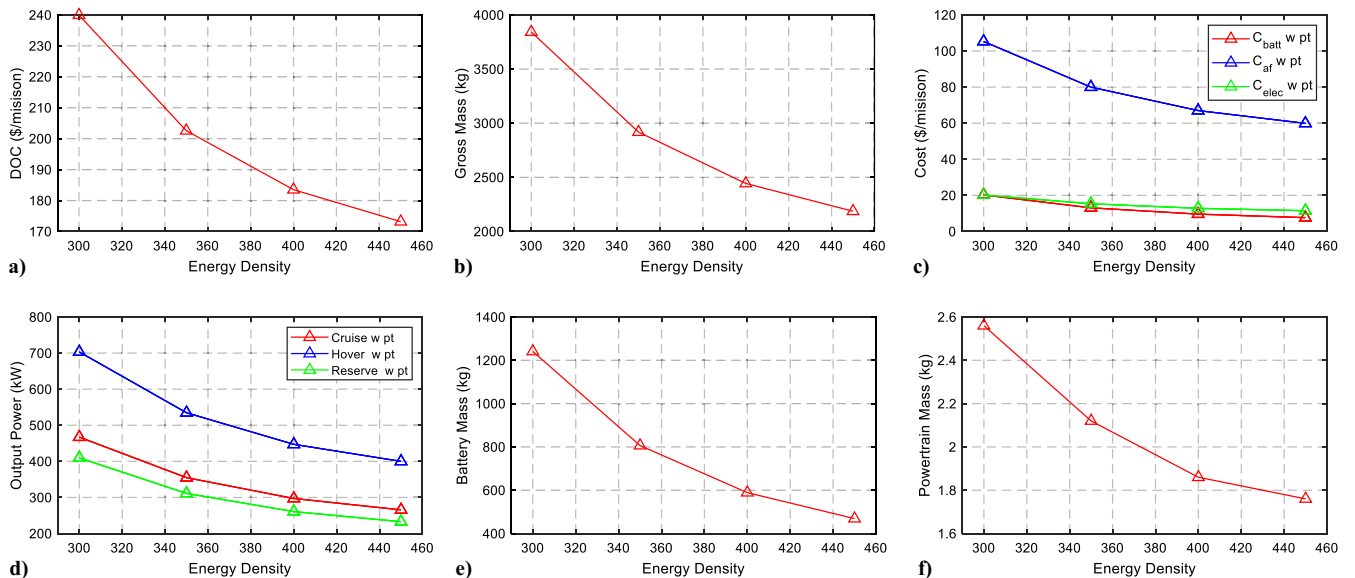


Fig. 12 Sensitivity to battery energy density. a) DOC. b) Gross mass. c) Depreciation cost. d) Output power. e) Battery mass. f) Powertrain mass.

implies that pursuing higher battery energy density may not always be beneficial.

Figure 13 demonstrates that as the battery life cycle increases, it has a significant impact on the cost of the battery itself but does not affect other components of the cost. Moreover, the optimal powertrain design remains unchanged despite variations in the battery life cycle.

Figure 14 illustrates how shifting parameters away from the optimal design setting impacts the overall cost function. In Figs. 14a and 14b, the switching frequency is swept from 61 to 151 kHz. The variation in switching frequency significantly impacts the performance of the powertrain system. As the switching frequency increases, the system's switching losses typically rise, leading to reduced efficiency and an increase in battery mass. Conversely, higher switching frequencies result in smaller passive components, reducing the overall mass of the powertrain. This creates a tradeoff between powertrain mass and battery mass. Figure 14a shows that as the switching frequency increases from

61 kHz, the overall DOC decreases, indicating that the impact of switching frequency on the powertrain dominates the variation, leading to a reduction in DOC. However, when the switching frequency exceeds the optimal design point, the influence of switching frequency on the battery becomes more significant, leading to an increase in the aircraft's gross mass and airframe mass, which further causes the DOC to increase again. Figure 14b provides a more detailed breakdown of how each cost component is affected by changes in switching frequency.

Figures 14c and 14d illustrate the impact of DC bus voltage on the system. When the DC bus voltage decreases, the current increases. Due to the constraints of maximum current density, the winding diameter becomes thicker and powertrain mass increases. Furthermore, as the current increases, the system's conduction losses increase, leading to reduced efficiency and an increase in battery mass. As a result, a decrease in DC bus voltage results in a higher DOC. Figure 14d provides a more detailed breakdown of how each cost component is affected by changes in DC bus voltage.

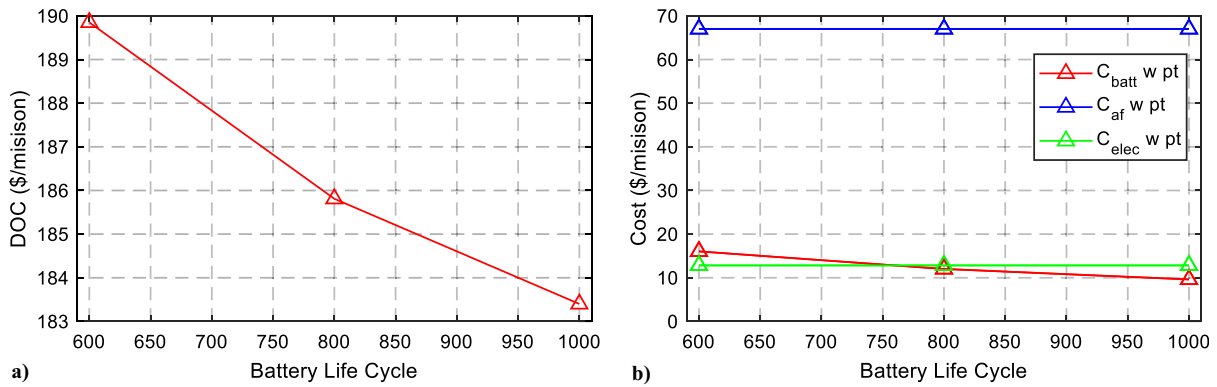


Fig. 13 Sensitivity to battery life cycle. a) DOC. b) Gross mass.

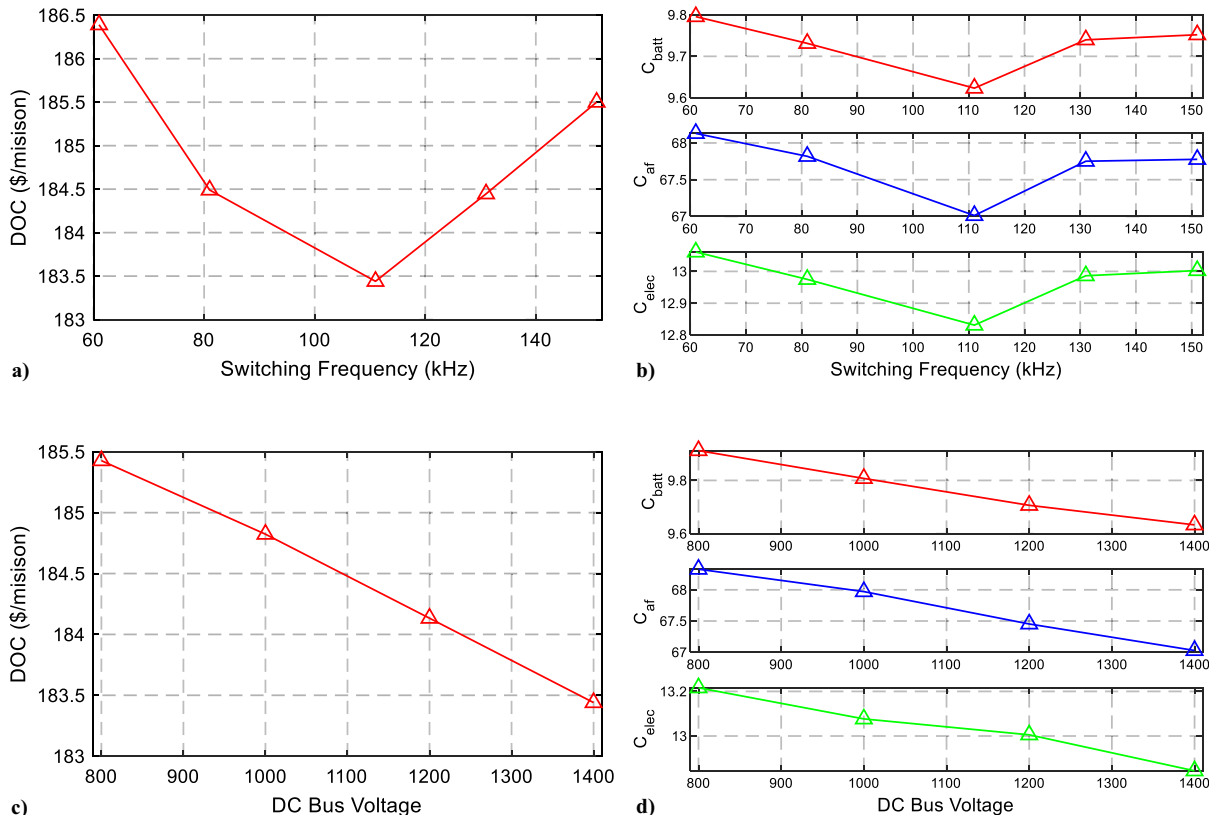


Fig. 14 Sensitivity to design space. a) Variation in DOC with switching frequency. b) Variation in main cost components with switching frequency. c) Variation in DOC with DC bus voltage. d) Variation in main cost components with DC bus voltage.

V. Conclusions

This work proposes a conceptual design and optimization methodology for eVTOL aircraft, with a focus on the powertrain aspect. Unlike most eVTOL aircraft optimizations, which either neglect the powertrain model or rely on basic equation-based models, this study introduces a comprehensive powertrain modeling methodology. Additionally, it performs a comparative study of models with and without a powertrain, highlighting the critical role of powertrain considerations in the optimization process for eVTOL aircraft design.

The cost per mission was used as the objective function in this study. The lift + cruise eVTOL aircraft was optimized under the selected mission profile. The two most important costs are pilot cost and battery cost. The keys to minimizing the cost per mission of eVTOL aircraft are implementing autonomous driving, reducing battery manufacturing costs, and increasing the battery life cycle. A case study of a 30 km cruise range in Los Angeles shows that the cost per mission can be optimized to \$165 per mission. Additionally, a comparison study was conducted in this work. The comparative analysis reveals that the proposed model is capable of achieving up to a 6.6% reduction in total DOC through powertrain and trajectory optimization. Sensitivity to mission range is analyzed, and it is observed that the impact of the powertrain on the eVTOL aircraft becomes more profound with an increase in range.

This paper quantitatively evaluates the influence of the powertrain system on eVTOL aircraft across various applications. Additionally, a comprehensive powertrain modeling methodology is introduced, aiming to provide guidance for individuals without a background in power electronics on constructing powertrain models for interdisciplinary applications.

Acknowledgment

The material presented in this paper is, in part, based upon work supported by NASA under award no. 80NSSC21M0070.

References

- [1] Moore, M. D., "Concept of Operations for Highly Autonomous Electric Zip Aviation," *12th AIAA Aviation Technology, Integration, and Operations (ATIO) Conference*, AIAA Paper 2012-5472, 2012. <https://doi.org/10.2514/6.2012-5472>
- [2] Asmer, L., Pak, H., Prakasha, P. S., Schuchardt, B. I., Weiland, P., Meller, F., Torens, C., Becker, D., Zhu, C., Schweiger, K., et al., "Urban Air Mobility use Cases, Missions and Technology Scenarios for the HorizonUAM Project," *AIAA Aviation Forum*, AIAA Paper 2021-3198, 2021. <https://doi.org/10.2514/6.2021-3198>
- [3] Boretti, A., "Advantages of Plug-In Hybrid Electric Vertical Take-Off and Landing Aircraft with Hydrogen Energy Storage," *International Journal of Hydrogen Energy*, Vol. 55, Dec. 2023, pp. 339–346. <https://doi.org/10.1016/j.ijhydene.2023.11.170>
- [4] Brown, A., and Harris, W. L., "Vehicle Design and Optimization Model for Urban Air Mobility," *Journal of Aircraft*, Vol. 57, No. 6, 2020, pp. 1003–1013. <https://doi.org/10.2514/1.C035756>
- [5] Scholz, A. E., Trifonov, D., and Hornung, M., "Environmental Life Cycle Assessment and Operating Cost Analysis of a Conceptual Battery Hybrid-Electric Transport Aircraft," *CEAS Aeronautical Journal*, Vol. 13, No. 1, 2022, pp. 215–235. <https://doi.org/10.1007/s13272-021-00556-0>
- [6] Critchfield, T., and Ning, A., "Low-Fidelity Design Optimization and Parameter Sensitivity Analysis of Tilt-Rotor eVTOL Electric Propulsion Systems," *AIAA SCITECH Forum*, AIAA Paper 2023-0325, 2023. <https://doi.org/10.2514/6.2023-0325>
- [7] Orndorff, N. C., Sarojini, D., Scotzniovsky, L., Gill, H., Lee, S., Cheng, Z., Zhao, S., Mi, C., and Hwang, J. T., "Air-Taxi Transition Trajectory Optimization with Physics-Based Models," *AIAA SCITECH Forum*, AIAA Paper 2023-0324, 2023. <https://doi.org/10.2514/6.2023-0324>
- [8] Ruh, M. L., Fletcher, A., Sarojini, D., Sperry, M., Yan, J., Scotzniovsky, L., van Schie, S. P., Warner, M., Orndorff, N. C., Xiang, R., et al., "Large-Scale Multidisciplinary Design Optimization of a NASA Air Taxi Concept Using a Comprehensive Physics-Based System Model," *AIAA SCITECH Forum*, AIAA Paper 2024-0771, 2024. <https://doi.org/10.2514/6.2024-0771>
- [9] Menzi, D., Imperiali, L., Bürgisser, E., Ulmer, M., Huber, J., and Kolar, J. W., "Ultra-Lightweight High-Efficiency Buck-Boost DC-DC Converters for Future eVTOL Aircraft with Hybrid Power Supply," *IEEE Transactions on Transportation Electrification*, Vol. 10, No. 4, 2024, pp. 10297–10313. <https://doi.org/10.1109/TTE.2024.3375026>
- [10] Nawawi, A., Tong, C. F., Yin, S., Sakanova, A., Liu, Y., Liu, Y., Kai, M., See, K. Y., Tseng, K.-J., Simanjorang, R., et al., "Design and Demonstration of High Power Density Inverter for Aircraft Applications," *IEEE Transactions on Industry Applications*, Vol. 53, No. 2, 2017, pp. 1168–1176. <https://doi.org/10.1109/TIA.2016.2623282>
- [11] Clarke, S., Redifer, M., Papathakis, K., Samuel, A., and Foster, T., "X-57 Power and Command System Design," *2017 IEEE Transportation Electrification Conference and Expo (ITEC)*, Inst. of Electrical and Electronics Engineers, New York, 2017, pp. 393–400. <https://doi.org/10.1109/ITEC.2017.7993303>
- [12] Liu, Y., See, K.-Y., Yin, S., Simanjorang, R., Tong, C. F., Nawawi, A., and Lai, J.-S. J., "LCL Filter Design of a 50-kW 60-kHz SiC Inverter with Size and Thermal Considerations for Aerospace Applications," *IEEE Transactions on Industrial Electronics*, Vol. 64, No. 10, 2017, pp. 8321–8333. <https://doi.org/10.1109/TIE.2017.2677338>
- [13] Sarojini, D., Ruh, M., Yan, J., Scotzniovsky, L., Orndorff, N. C., Xiang, R., Zhao, H., Krokowski, J., Warner, M., van Schie, S., et al., "Review of Computational Models for Large-Scale MDAO of Urban Air Mobility Concepts," *AIAA SciTech Forum*, AIAA Paper 2024-0377, 2024. <https://doi.org/10.2514/6.2024-0377>
- [14] Ouyang, Z., and Andersen, M. A., "Overview of Planar Magnetic Technology—Fundamental Properties," *IEEE Transactions on Power Electronics*, Vol. 29, No. 9, 2013, pp. 4888–4900. <https://doi.org/10.1109/TPEL.2013.2283263>
- [15] Burkart, R. M., "Advanced Modeling and Multi-Objective Optimization of Power Electronic Converter Systems," Ph.D. Thesis, ETH Zurich, 2016, https://www.pes-publications.ee.ethz.ch/uploads/tx_ethpublications/Thesis_Burkart_MOO_final.pdf
- [16] Li, J., Abdallah, T., and Sullivan, C. R., "Improved Calculation of Core Loss with Nonsinusoidal Waveforms," *Conference Record of the 2001 IEEE Industry Applications Conference. 36th IAS Annual Meeting (Cat. No. 01CH37248)*, Vol. 4, Inst. of Electrical and Electronics Engineers, New York, 2001, pp. 2203–2210. <https://doi.org/10.1109/IAS.2001.955931>
- [17] National Energy Technology Laboratory, "Core-Loss Datasheet MnZn Ferrite N87," Tech. Rept., DOE, Sept. 2018, <https://www.netl.doe.gov/sites/default/files/netl-file/Core-Loss-Datasheet---MnZn-Ferrite---N87%5B1%5D.pdf>
- [18] National Energy Technology Laboratory, "METGLAS-2605-SA1 Core-Loss Datasheet," Tech. Rept., U.S. Department of Energy—National Energy Technology Laboratory, Morgantown, WV, 2018, https://www.netl.doe.gov/sites/default/files/netl-file/METGLAS-2605-SA1-Core-Datasheet_approved%5B1%5D.pdf
- [19] Mühlethaler, J., "Modeling and Multi-Objective Optimization of Inductive Power Components," Ph.D. Thesis, ETH Zurich, Zürich, Switzerland, 2012. <https://doi.org/10.3929/ethz-a-007328104>
- [20] Zou, J., Brooks, N. C., Coday, S., Ellis, N. M., and Pilawa-Podgurski, R. C., "On the Size and Weight of Passive Components: Scaling Trends for High-Density Power Converter Designs," *2022 IEEE 23rd Workshop on Control and Modeling for Power Electronics (COMPEL)*, Inst. of Electrical and Electronics Engineers, New York, 2022, pp. 1–7. <https://doi.org/10.1109/COMPEL53829.2022.9829957>
- [21] Gammeter, C., Krismer, F., and Kolar, J. W., "Weight Optimization of a Cooling System Composed of Fan and Extruded-Fin Heat Sink," *IEEE Transactions on Industry Applications*, Vol. 51, No. 1, 2014, pp. 509–520. <https://doi.org/10.1109/TIA.2014.2336977>
- [22] Wang, P., McCluskey, P., and Bar-Cohen, A., "Two-Phase Liquid Cooling for Thermal Management of IGBT Power Electronic Module," *Journal of Electronic Packaging*, Vol. 135, No. 2, 2013, Paper 021001. <https://doi.org/10.1115/1.4023215>
- [23] Silva, C., and Johnson, W., "Practical Conceptual Design of Quieter Urban VTOL Aircraft," *Vertical Flight Society's 77th Annual Forum & Technology Display*, F-0077-2021-16739, Vertical Flight Soc., 2021. <https://doi.org/10.4050/F-0077-2021-16739>
- [24] "14 CFR 91.151—Fuel Requirements for Flight in VFR Conditions," Dept. of Transportation, Federal Aviation Administration, 2017, <https://www.law.cornell.edu/cfr/text/14/91.151> [retrieved 14 Aug. 2019].

- [25] Thorbeck, J., and Scholz, D., "DOC-Assessment Method," *Proceedings of the 3rd Symposium on Collaboration in Aircraft Design*, Vol. 19, CEAS Technical Committee Aircraft Design (CEAS TCAD), Toulouse, France, 2013, https://www.fzt.haw-hamburg.de/pers/Scholz/Aero/TU-Berlin_DOC-Method_with_remarks_13-09-19.pdf.
- [26] Scholz, A. E., Trifonov, D., and Hornung, M., "Environmental Life Cycle Assessment and Operating Cost Analysis of a Conceptual Battery Hybrid-Electric Transport Aircraft," *CEAS Aeronautical Journal*, Vol. 13, No. 1, 2022, pp. 215–235. <https://doi.org/10.1007/s13272-021-00556-0>
- [27] Dept. of Transportation, Federal Aviation Administration, "Labor Cost Factors and Economic Value Guidance," Tech. Rept. Federal Aviation Administration (FAA), Jan. 2025, https://www.faa.gov/sites/faa.gov/files/regulations_policies/policy_guidance/benefit_cost/econ-value-section-7-labor-cost-factors.pdf.
- [28] "Airline Disclosure Guide: Aircraft Acquisition Cost and Depreciation," International Air Transport Association (IATA), 2024, <https://www.iata.org/contentassets/4a4b100c43794398baf73dcea6b5ad42/airline-disclosure-guide-aircraft-acquisition.pdf> [retrieved 22 July 2024].
- [29] Dong, Q., Liang, S., Li, J., Kim, H. C., Shen, W., and Wallington, T. J., "Cost, Energy, and Carbon Footprint Benefits of Second-Life Electric Vehicle Battery use," *iScience*, Vol. 26, No. 7, 2023, Paper 107195. <https://doi.org/10.1016/j.isci.2023.107195>
- [30] Engel, H., Hertzke, P., and Siccardo, G., "Second-Life EV Batteries: The Newest Value Pool in Energy Storage," 2019, <https://www.mckinsey.com/industries/automotive-and-assembly/our-insights/second-life-ev-batteries-the-newest-value-pool-in-energy-storage>, McKinsey & Company.
- [31] Fraunhofer, I., "Technologie-Roadmap Energiespeicher für Die Elektromobilität 2030," 2012, <https://www.econstor.eu/bitstream/10419/66521/1/729050173.pdf>.
- [32] U.S. Bureau of Labor Statistics, "Average energy prices for the United States, regions, census divisions, and selected metropolitan areas," *EB/OL*, 2024, https://www.bls.gov/regions/midwest/data/averageenergyprices_selectedareas_table.htm [retrieved 18 June 2024].
- [33] Gudmundsson, S., "General Aviation Aircraft Design: Applied Methods and Procedures," Butterworth-Heinemann, 2013, <https://www.elsevier.com/books/general-aviation-aircraft-design/gudmundsson/978-0-12-397308-5>.
- [34] United Airlines and International Brotherhood of Teamsters, "Mechanics and Related Review of Economic Highlights in February 2024 Contract Extension TA," Tech. Rept., Teamsters Union, 2024, <https://teamster.org/wp-content/uploads/2024/03/United-Airlines-%E2%80%93-Mechanics-and-Related-Review-of-Economic-Highlights-in-February-2024-Contract-Extension-TA.pdf>.
- [35] Raymer, D., *Aircraft Design: A Conceptual Approach*, AIAA, Reston, VA, 2012, Chap. 18. <https://doi.org/10.2514/4.869112>
- [36] "LADOT Aerial Mobility Report," Los Angeles Dept. of Transportation, 2024, <https://ladot.lacity.gov/aerialmobilityreport> [retrieved 10 June 2024].
- [37] "Charter Helicopter Flight from Burbank Airport to LAX," Orbic Air, 2024, <https://orbicair.com/i-7335338-charter-helicopter-flight-from-burbank-airport-to-lax.html> [retrieved 10 June 2024].

J. Kuchar
Associate Editor